Astronomy & Astrophysics manuscript no. AA202348263
November 22, 2023

Analysis of the public HARPS/ESO spectroscopic archive

Ca II H&K time series for the HARPS radial velocity database

V. Perdelwitz[1,2,5], T. Trifonov[3,4,6], J. T. Teklu[5], K. R. Sreenivas[5], and L. Tal-Or[5,7]

[1] Department of Earth and Planetary Science, Weizmann Institute of Science, Rehovot, Israel
e-mail: volker.perdelwitz@weizmann.ac.il
[2] Hamburger Sternwarte, Universität Hamburg, Gojenbergsweg 112, 21029 Hamburg, Germany
[3] Department of Astronomy, Faculty of Physics, Sofia University "St. Kliment Ohridski", 5 James Bourchier Blvd., BG-1164 Sofia, Bulgaria
[4] Max-Planck-Institut für Astronomie, Königstuhl 17, 69117 Heidelberg, Germany
[5] Department of Physics, Ariel University, Ariel 40700, Israel
[6] Zentrum für Astronomie der Universtät Heidelberg, Landessternwarte, Königstuhl 12, 69117 Heidelberg, Germany
[7] Astrophysics Geophysics And Space Science Research Center, Ariel University, Ariel 40700, Israel

Received 13/10/2023; accepted —

ABSTRACT

Context. Magnetic activity is currently the primary limiting factor in radial velocity (RV) exoplanet searches. Even inactive stars, such as the Sun, exhibit RV jitter on the order of a few m s^{-1} due to active regions on their surfaces. Time series of chromospheric activity indicators, such as the Ca II H&K lines, can be utilized to reduce the impact of such activity phenomena on exoplanet search programs. In addition, the identification and correction of instrumental effects can improve the precision of RV exoplanet surveys.
Aims. We aim to update the HARPS-RVBank RV database, previously published by Trifonov et al. (2020), and include additional 3.5 years of time series and Ca II H&K lines ($R'_{\rm HK}$) chromospheric activity indicators. This additional data will aid in the analysis of the impact of stellar magnetic activity on the RV time series obtained with the HARPS instrument. Our updated database aims to provide a valuable resource for the exoplanet community in understanding and mitigating the effects of such stellar magnetic activity on RV measurements.
Methods. The new HARPS-RVBank database includes all stellar spectra obtained with the HARPS instrument prior to January 2022. The RVs corrected for small but significant nightly zero-point variations were calculated using the same method described in Trifonov et al. (2020). The $R'_{\rm HK}$ estimates were determined from both individual spectra and co-added template spectra using the methodology outlined in Perdelwitz et al. (2021), which utilizes synthetic model spectra. As input for our derivation of $R'_{\rm HK}$, we derived stellar parameters from coadded, high-SNR templates for a total of 3 849 stars using the stellar parameter code SPECIES (Soto & Jenkins 2018; Soto et al. 2021).
Results. The new version of the HARPS RV database has a total of 252 615 RVs of 5 239 stars. Of these, 200 774 have $R'_{\rm HK}$ values, which corresponds to 80% of all publicly available HARPS spectra. Currently, this is the largest public database of high-precision (down to $\sim$ 1 m s^{-1}) RVs, and the largest compilation of $R'_{\rm HK}$ measurements. We also derive lower limits the RV jitter of F-, G- and K-type stars as a function of $R'_{\rm HK}$.

Key words. stars: activity – planetary systems – techniques: radial velocities – stars: late-type

1. Introduction

While the transit method has led to the detection of a greater number of exoplanets compared to the radial velocity (RV) method, the RV technique remains a valuable tool in the detection and characterization of exoplanetary companions. This is because it does not require continuous observations over multiple planetary periods, enabling the discovery of planets with orbital periods on the order of the time span over which spectra have been collected. This time span can be several decades for stars observed by multiple facilities. As such, the RV method enables the creation of a representative sample of planetary companions without the need for continuous coverage.

The yield of a search for substellar companions via the radial velocity method using high-resolution spectrographs such as HARPS (Mayor et al. 2003) is increased by optimizing the RV extraction method (e.g., Zechmeister et al. 2018) and by correcting the RVs for nightly instrumental effects (e.g., Courcol et al. 2015; Tal-Or et al. 2019). Based on the publicly available HARPS spectra Trifonov et al. (2020) published the HARPS-RVBank, a catalogue of > 212 000 corrected RVs, which have since been used by the community to confirm or discover planet candidates (e.g., Palatnick et al. 2021; Sreenivas et al. 2021) and estimate planet occurrence rates (Bashi et al. 2020).
Aside from the detrimental influence of instrumental effects, stellar magnetic activity has been known for a long time to be the primary cause of radial velocity jitter (Saar et al. 1998). In combination with stellar rotation, the presence of active regions on the stellar surface can result in quasi-periodic RV signals mimicking those caused by a substellar companion (Queloz et al. 2001; Dumusque et al. 2011; Reiners et al. 2013). While this RV noise is larger in younger and more active stars (Tal-Or et al. 2018; Brems et al. 2019), it has a more complex dependence on spectral type (Dumusque et al. 2011). Even slow rotators with low levels of magnetic activity, such as our Sun, exhibit

RV jitter of few m s^{-1} (Marchwinski et al. 2015; Haywood et al. 2016; Collier Cameron et al. 2019), thus exceeding the nominal precision of state-of-the-art planet-hunting facilities such as ESPRESSO (Pepe et al. 2014), and upcoming facilities.

Though efforts have been made to mitigate the effect of magnetic activity with various methods (Collier Cameron et al. 2021; Binnenfeld et al. 2021), to this date, the most reliable way to exclude false positive detections is to measure the stellar rotation period and demonstrate it to be different from the planetary candidate signal. This can be achieved by analysing photospheric activity indicators (i.e. light curves, McQuillan et al. 2014), or chromospheric lines such as Hα or Ca II H&K (e.g., Amado et al. 2021). In this publication, we present an update of the HARPS-RVBank, which incorporates newly available observational data, including 252 615 RVs of 5 239 stars and measurements of the relative emission in the Ca II H&K lines, $R'_{\rm HK}$, for 80% of all spectra. In Sect. 2, we provide details of our re-processing scheme with the SERVAL pipeline, the Nightly Zero Point (NZP) correction process, and the derivation of stellar parameters and R'HK from the public spectra. In Sect. 3, we present our results and provide discussion of our findings. Finally, in Sect. 4, we present a summary and our conclusions.

2. Updating the HARPS-RVBank

We obtained all available HARPS stellar spectra from the ESO archive (http://archive.eso.org/wdb/wdb/adp/phase3_main/form) that were observed prior to January 2022. These spectra were processed in the same manner as described in Trifonov et al. (2020). In addition to the data reduction software (DRS) products provided by HARPS, we calculated SERVAL RVs and various activity indices using the methodology described in Zechmeister et al. (2018, 2020). We also determined the data-driven NZP corrections for both the DRS and SERVAL RVs, which improves the overall precision of the HARPS measurements.

In the first release of the HARPS-RVBank, we only included targets with at least three usable spectra, as this was the minimum required for constructing a spectral template and obtaining precise RVs with SERVAL. In this second release of the HARPS-RVBank, we have extended the inclusion criteria to include targets with a single usable spectrum, significantly increasing the number of targets. While we cannot compute meaningful SERVAL RVs and activity indices for these targets, we provide the original HARPS-DRS estimates and use their spectra to estimate Ca II H&K values, which is the primary focus of this work. From 2003 to the present, we retrieved 309,425 unique spectra from the ESO archive. Of these spectra, 12,136 were excluded due to their classification as solar spectra, solar system objects, QSOs, and various transients. Additionally, 36,765 spectra were not included in the HARPS-RVBank due to failing the quality control check, which includes criteria such as being taken with an I2 cell, having extremely low or high S/N, or exhibiting other issues that prevent the extraction of meaningful results. The new HARPS-RVBank consists of 252 615 unique spectra of 5 239 targets[1] that have passed the semi-automated quality control process (see, Trifonov et al. 2020, for details).

[1] Instant access to the HARPS-RVBank products is made available through the Exo-Striker exoplanet toolbox (Trifonov 2019), which can be freely accessed at https://github.com/3fon3fonov/exostriker.

2.1. Adding NZP-corrected RVs

The NZP correction of the RVs was performed as described in Tal-Or et al. (2019) and Trifonov et al. (2020), where more detailed descriptions of the algorithm can be found. In short, we calculated NZPs for all nights in which at least three different RV-quiet stars (stars with RV scatter < 10 m s^{-1}) were observed. This was done by taking the weighted average of their RVs, after subtracting from each star its own weighted-average RV (stellar zero point). To properly weight the contribution of each star to the NZP timeseries, the stellar zero-point uncertainty of each star was co-added (in quadrature) to its RV errors. The stellar zero-point uncertainty of each star was taken as either its mean RV uncertainty or its RV rms scatter, the higher of the two. This way, the contribution of variable and active stars is properly downweighted in calculating the NZPs.

Figures 1 and 2 show the zero-point variations and the average intra-night drift of post-SERVAL RVs, respectively. Despite the 2020–2021 COVID-related observing gaps the instrument's zero-point behaviour does not differ much from what was reported in Trifonov et al. (2020). The 774 good NZPs (out of 1395 nights with useful data) have a weighted rms scatter of 1.8 m s^{-1} and a median error of 1.1 m s^{-1}, which demonstrates the significance of the correction. Interestingly, the night-to-night variations are accompanied by a small average (< 1 m s^{-1} peak-to-peak) positive intra-night drift, which is absent from HARPS-pre SERVAL RVs.

Figure 3 shows the standard deviation of RV-quiet star RVs before and after correcting for nightly zero point variations and the average intra-night drift. For inactive stars with $\sigma_{RV} \leq 3$ m s^{-1}, the NZP correction slightly improves RV jitter, which is evident from most of the points being below the 1:1 line. This may become useful for finding low-mass planets. As discussed in Trifonov et al. (2020), for some stars the DRS RVs may have a better precision than the SERVAL RVs due to various reasons. For in-depth analysis of specific stars one may apply their own RV derivation scheme to the spectra, and check whether applying the NZP correction values, as given in the HARPS-RVBank, improve them. RV time series quality is ultimately measured by their predictive power, not by their RV rms scatter, particularly for periodic signals.

2.2. Derivation of stellar parameters

The approach developed by Perdelwitz et al. (2021) requires precise stellar parameters, namely effective temperature ($T_{\rm eff}$), surface gravity ($\log g$), metallicity ([Fe/H]), and rotational velocity ($v \sin i$). In order to ensure that the parameters are derived in as homogeneously a manner as possible, we used the publicly available code SPECIES[2] (Soto & Jenkins 2018; Soto et al. 2021). The single-exposure HARPS spectra for each target were shifted to rest-frame and co-added. Only the resulting templates with an SNR ≥ 20 were then processed with SPECIES, using the default line lists implemented in the code. Fig. 4 shows the distribution of SNR of all template spectra.

Out of a total of 5 239 stars in the sample, we were able to derive stellar parameters for 3 849. The discrepancy is caused in most cases by a low SNR of the coadded spectrum, or stellar contamination by a close companion in others. Figures 5, 6 and 7 show the comparison of the resulting effective temperature, surface gravity and metallicity with those published in the latest version of the TESS input catalogue (TIC v8.2 Stassun et al.

[2] https://github.com/msotov/SPECIES

Table 1: Stellar parameters. The full table is available on the CDS.

Name	ra [deg]	dec [deg]	T_{eff} [K]	ΔT_{eff} [K]	log g	Δlog g	[Fe/H] [dex]	Δ[Fe/H] [dex]	v sini [km s^{-1}]	Δv sini [km s^{-1}]	R'_{HK}	$\Delta R'_{HK}$	vflag
BD+012494	163.0321195	0.49329	5524	50	4.1	0.1	0.29	0.042	4.0	0.3	$1.07\cdot10^{-5}$	$5.63\cdot10^{-7}$	0
BD+01316	26.63371	2.69887	6370	50	4.2	0.1	0.26	0.047	5.5	0.4	$6.98\cdot10^{-6}$	$3.59\cdot10^{-7}$	0
BD+034525	318.47394	4.45293	5754	61	4.1	0.1	0.05	0.05	3.9	0.2	$8.80\cdot10^{-5}$	$1.61\cdot10^{-5}$	0
BD+053805	278.947839	5.33738	5163	50	3.0	0.1	-0.09	0.043	4.2	0.4	$6.49\cdot10^{-6}$	$6.87\cdot10^{-7}$	0

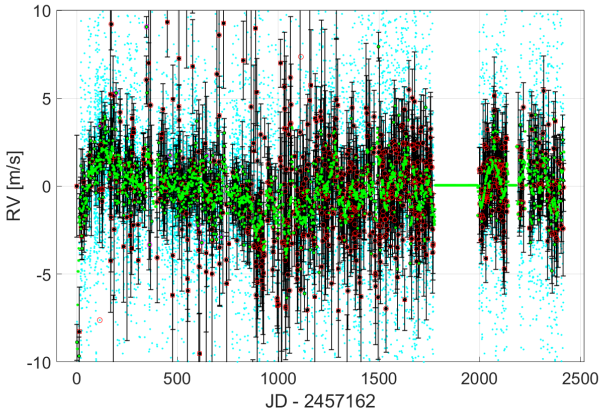

Fig. 1: *Black errorbars*: HARPS-post SERVAL NZPs. *Cyan dots*: stellar zero-point subtracted RVs of all RV-quiet stars (weighted RV rms scatter $< 10\,\mathrm{m\,s^{-1}}$). *Red boxes*: NZPs that were calculated with too few (< 3) RVs. *Red circles*: NZPs with too large uncertainties ($> 1.2\,\mathrm{m\,s^{-1}}$). *Magenta circles*: significantly deviating NZPs. The RVs in the red-marked nights are corrected by using a smoothed version of the NZP curve, which was calculated with a moving weighted average (21-d window). For the ten significantly deviating NZPs, we adopted their individual (unsmoothed) NZP values, regardless of their uncertainties. *Green dots*: the NZP values that were eventually used for the correction.

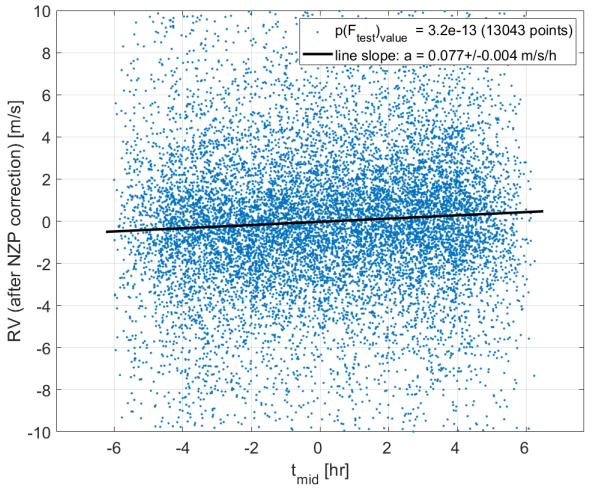

Fig. 2: The average nightly drift in HARPS-post SERVAL RVs.

2019). While there is generally a good agreement between the sets of parameters, we do advise that systematic errors in any derivation of stellar parameters may be larger than measured uncertainties (Torres et al. 2012).

The sample of targets for which all stellar parameters have been

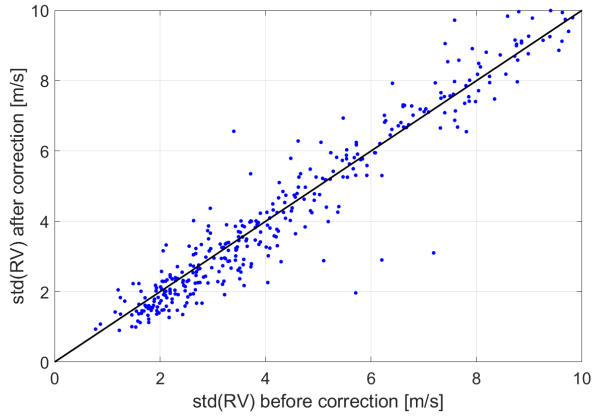

Fig. 3: Comparison of the standard deviation in RV before and after the new zero point correction.

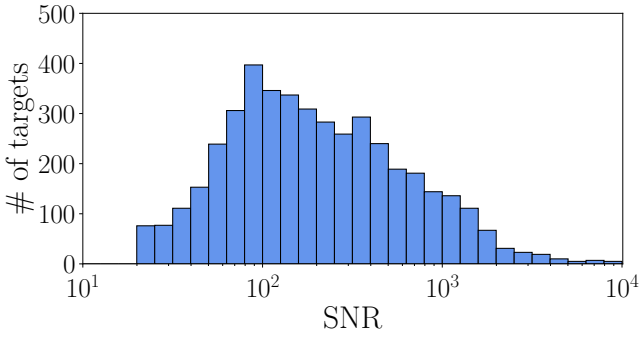

Fig. 4: Distribution of the SNR of spectral templates used to compute stellar parameters.

derived solely based on the HARPS spectra corresponds to a total of 172,948 single spectra, or 68.6% of the total. In order to increase this fraction, the remaining stars were cross-matched with the TESS input catalogue, which contains effective temperature, surface gravity, and metallicity, but no rotational velocity. We, therefore, crossmatched the remaining sources with the Gaia DR3 catalogue (Gaia Collaboration et al. 2021a,b), yielding an additional 54 rotational velocity values. In the stellar parameter catalogue published along with this appear (see Table 1), which is available at the CDS[3], these targets are marked with $vflag = 2$, those without any rotational velocity with $vflag = 1$.

2.3. Extraction of R'_{HK}

We follow the recipe of Perdelwitz et al. (2021), namely the computation of a grid of fluxes in six bands from PHOENIX models

[3] https://cdsarc.cds.unistra.fr/viz-bin/cat/J/A+A/vvv/App

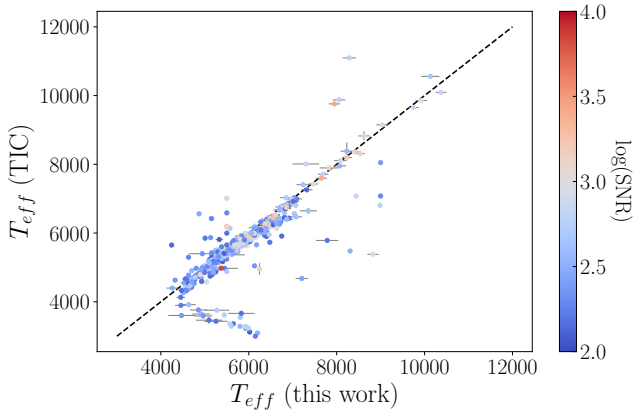

Fig. 5: Comparison of effective temperature with literature values. The y-axis represents the values published in Stassun et al. (2019), and the black dashed line represents equality. Note that the apparent tail of deviations towards lower temperatures comprises of stars for which the radial velocity was not known, and for which the stellar parameter determination failed. All stars with missing RV value and possible errors in the catalogue are marked via the VFLAG column in our catalogue.

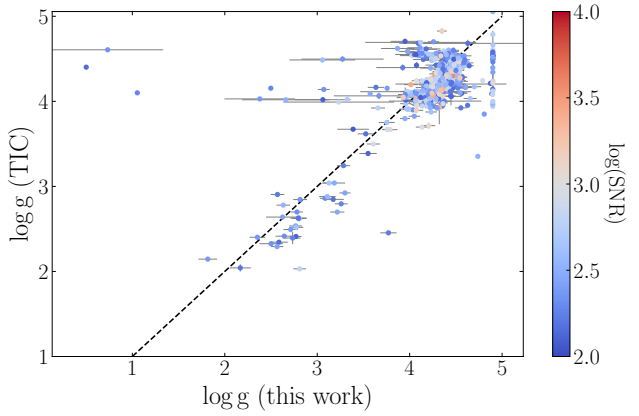

Fig. 6: Comparison of surface gravity with literature values. The y-axis represents the values published by Stassun et al. (2019), the black dashed line represents equality.

(Husser et al. 2013), with varying $T_{\rm eff}$, $\log g$ and [Fe/H], where grid step size follows that of the PHOENIX grid (see Table 1 in Husser et al. 2013). We adapted the edges of one bandpass (k_1) with respect to those used in Perdelwitz et al. (2021) in order to minimize the number of absorption lines and hence the influence of errors caused by the determination of stellar metallicity. Tab. 2 lists the updated bandpasses, and fig. 8 displays the bandpasses for three example model spectra. In addition to the parameters given by the PHOENIX grid, the spectra were artificially broadened with velocities in the range 1-200 km s^{-1} in order to account for stellar rotation. The measured spectra were then rectified in the regions of the Ca II H&K lines and flux normalized, the photospheric contribution in the lines was subtracted, and the resulting chromospheric excess was normalized with the bolometric flux, yielding $R'_{\rm HK}$. As mentioned in 2.2, for some stars in the stellar parameter catalogue we were not able to determine $v \sin i$. During data reduction, $v \sin i$ was set to 2 km s^{-1} for these targets. While the time series of these stars can be used to determine rotation periods or activity cycles, $R'_{\rm HK}$ of these stars may be biased, which is why these entries are marked with the *vflag* in both the stellar parameter and the time series table. We determined $R'_{\rm HK}$ for two sets of spectra:

(i): Individual measurements. To provide time series for individual targets, these values and their uncertainties are included as additional columns in the updated HARPS-RVBANK. Since the purpose of the single-measurement catalogue is the study of the

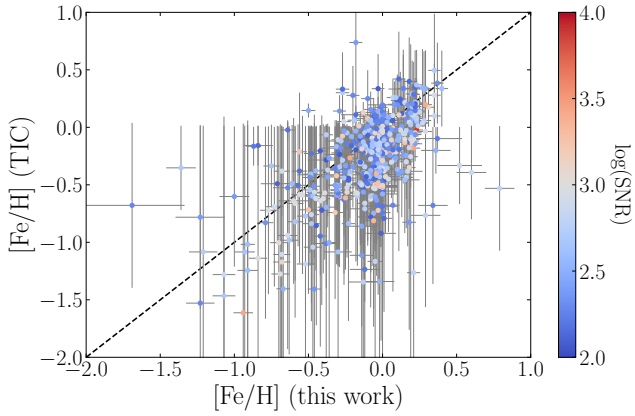

Fig. 7: Comparison of metallicity with literature values. The y-axis represents the values published by Stassun et al. (2019), the black dashed line represents equality.

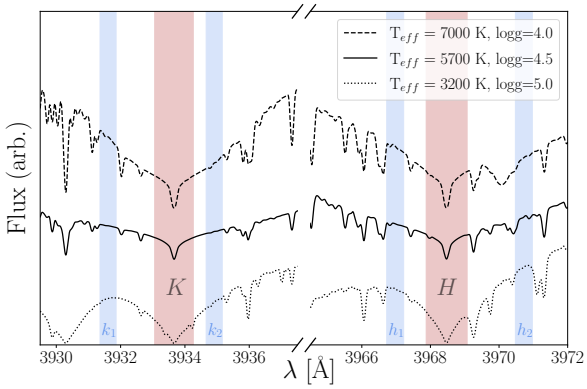

Fig. 8: Wavelength bands used for normalization and rectification of the spectra. The black lines show three examples of PHOENIX spectra with different stellar parameters.

Table 2: Updated wavelength bands used for rectification and flux extraction. The changes with respect to Perdelwitz et al. (2021) are highlighted.

Band	Wavelength range $[\lambda_{\rm min}, \lambda_{\rm max}]^a$
K	$[\lambda_K - 0.6$ Å, $\lambda_K + 0.6$ Å$]$
H	$[\lambda_H - 0.6$ Å, $\lambda_H + 0.6$ Å$]$
$\mathbf{k_1}$	$[\lambda_K$**−2.3** Å, λ_K**−1.8** Å$]$
k_2	$[\lambda_K + 2.5$ Å, $\lambda_K + 3.0$ Å$]$
h_1	$[\lambda_H - 1.75$ Å, $\lambda_H - 1.25$ Å$]$
h_2	$[\lambda_H + 2.0$ Å, $\lambda_H + 2.5$ Å$]$

Notes. [(a)] Central wavelengths: $\lambda_K = 3933.66$ Å, $\lambda_H = 3968.47$ Å.

time series of individual stars, $\Delta R'_{\rm HK}$ was derived purely based on the uncertainty in flux.

(ii): Co-added templates. To obtain an averaged, high-SNR value per target, the resulting $R'_{\rm HK}$ are listed in the catalogue of stellar parameters described in Sec. 2.2. In order to allow for a comparison of the average activity levels of different stars, here, the uncertainties of the stellar parameters were included in the Monte Carlo approach for the error estimation.

3. Results and Discussion

Our analysis resulted in a total of 200 755 $R'_{\rm HK}$ measurements, or ~ 80% of the entire HARPS RVBank. In the following, we give a short discussion of the relationship between $R'_{\rm HK}$ and RV jitter, and compare our findings to previous results. Tab. 3 gives an overview of the statistics of the parameter derivation.

Table 3: Overview of the number of spectra, and the source of the stellar parameters used for the derivation of $R'_{\rm HK}$

Sample	number of spectra
total # of HARPS spectra	252615
$R'_{\rm HK}$ derived with SPECIES parameters	172948
$R'_{\rm HK}$ derived with TIC parameters	27807
Total	200755

3.1. RV jitter as a function of activity and spectral type

The number of stars of spectral types F, G and K in the sample is large enough to derive lower limits on the RV jitter as a function of spectral type and activity level. Figure 9 shows the radial velocity jitter σ_{RV} as a function of $R'_{\rm HK}$ derived from the co-added spectra for all main sequence stars of spectral types F, G or K in the sample with at least 20 individual measurements. Here, we also excluded binaries with an RV jitter of $\sigma_{RV} > 200$ m s^{-1}. For each spectral type, the sample was subdivided into activity levels with step sizes of 0.25 in $\log(R'_{\rm HK})$, and the 10^{th} percentile of all radial velocities was adopted as the lower limit for each bin.

We derive the best-fit linear approximation for the lower limit of radial velocity jitter of F-type stars to be:

$$\log \sigma_{RV}[\mathrm{m\,s^{-1}}] = 0.74 \times \log R'_{\rm HK} + 3.98, \quad (1)$$

for G-type:

$$\log \sigma_{RV}[\mathrm{m\,s^{-1}}] = 0.82 \times \log R'_{\rm HK} + 4.47, \quad (2)$$

and for K dwarfs:

$$\log \sigma_{RV}[\mathrm{m\,s^{-1}}] = 0.99 \times \log R'_{\rm HK} + 5.43. \quad (3)$$

3.2. Comparison to previous publications

Gomes da Silva et al. (2021) recently published a catalogue of chromospheric activity for a sample of 1674 FGK stars based on HARPS data. Since the underlying spectra are entirely included in our dataset, we compare the median $R'_{\rm HK}$ from their catalogue to that derived from our template spectra. Fig. 10 shows that there are two types of systematic offset: *(i)* Cooler stars appear more active and *(ii)* most inactive stars exhibit lower $R'_{\rm HK}$ in our

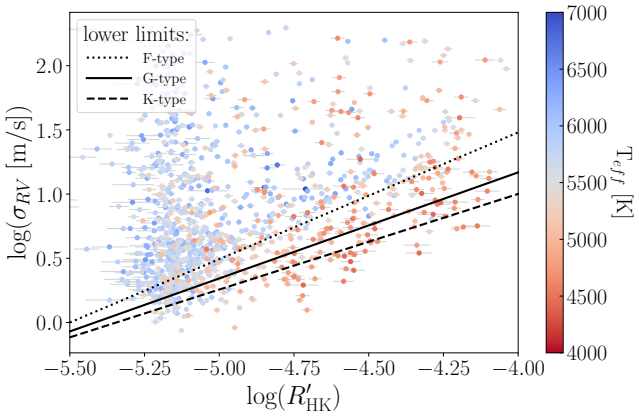

Fig. 9: Radial velocity jitter as a function of activity. The colour coding denotes the spectral type, and the dotted, solid and dashed line the lower RV jitter for spectral types F, G, and K, respectively.

catalogue, both relative to the values given by Gomes da Silva et al. (2021). While identifying the source of these systematics is beyond the scope of this paper, we tentatively conclude that it originates in the different methods for the extraction of $R'_{\rm HK}$. Our approach takes into account all stellar parameters including metallicity and rotational velocity, whereas the standard method of deriving $R'_{\rm HK}$, as carried out in Gomes da Silva et al. (2021), is the extraction of the Mount Wilson S-Index, which is subsequently converted to the excess chromospheric emission using a conversion based solely on the stellar colour ($B - V$).

Neglecting some stellar parameters in extracting $R'_{\rm HK}$ may be an oversimplification. For example, Schröder et al. (2009) found that fast stellar rotation leads to a filling-in of the Ca II H&K lines, thus increasing the flux as determined by the classical Mount Wilson method. Furthermore, it has been found that $R'_{\rm HK}$ is dependent on stellar metallicity (Saar & Testa 2012). We conclude that any derivation of $R'_{\rm HK}$ via a conversion factor which depends only on the stellar colour will likely be biased. Furthermore, as described in Perdelwitz et al. (2021), the method of using narrow bands close to the cores of the Ca II lines to rectify and normalize the spectra, while resulting in larger statistical errors compared to the classical approach, is less prone to systematics caused by irregularities in the order-merging or normalization of the pipeline-reduced spectra.

4. Summary and conclusions

We present an update of the HARPS-RVBank with newly calculated RVs, nightly zero points, and an addition of $R'_{\rm HK}$ for 80% of all spectra. Table 4 shows an example of five (out of 252 615) rows of the full catalogue. For 4361 stars, we were able to derive stellar parameters using co-added template spectra, which are available as a separate table. The updated radial velocities will enable the detection of new planet candidates in the same manner as the previous version of the HARPS-RVBank (e.g. Feng et al. 2020; Sreenivas et al. 2021). The addition of the relative chromospheric emission in the Ca II H&K lines, $R'_{\rm HK}$, provides an additional tool for the study of stellar magnetic activity and the identification of false-positive planet detections caused by stellar rotation. The updated HARPS-RVBank has already been used in several works on planet detection (Trifonov et al. 2022), stellar activity jitter (Kossakowski et al. 2022) and magnetic activity

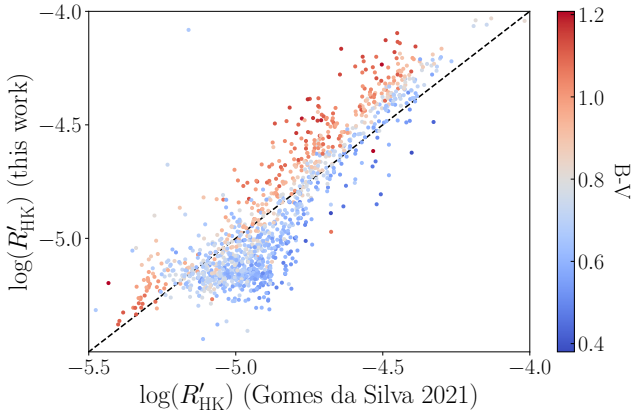

Fig. 10: Comparison of our median R'_{HK} values to those derived by Gomes da Silva et al. (2021). The colour coding denotes B-V.

cycles (Fuhrmeister et al. 2022). While our R'_{HK} values show colour-dependent systematic deviations compared to those derived with in the classical way, i.e. via the S-Index, we conclude that this is caused by the simplification made in the conversion with a factor that is solely a function of stellar colour $B - V$.

Acknowledgements. V.P. acknowledges funding through the Kimmel prize fellowship of the Center for Earth and Planetary Science at the Weizmann Institute of Science, and the Dean's fellowship of the faculty of chemistry (WIS). T.T. acknowledge support by the BNSF program "VIHREN-2021" project No. KP-06-DV-5/15.12.2021. T.T. acknowledges support by the DFG Research Unit FOR 2544 "Blue Planets around Red Stars" project No. KU 3625/2-1. This work was also funded by the Israel Science Foundation through grant No. 1404/22.

Based on observations made with ESO Telescopes at the La Silla Paranal Observatory under programme IDs 0100.C-0097, 0100.C-0111, 0100.C-0414, 0100.C-0474, 0100.C-0487, 0100.C-0708, 0100.C-0746, 0100.C-0750, 0100.C-0808, 0100.C-0836, 0100.C-0847, 0100.C-0884, 0100.C-0888, 0100.D-0176, 0100.D-0273, 0100.D-0339, 0100.D-0444, 0100.D-0535, 0100.D-0776, 0101.C-0106, 0101.C-0232, 0101.C-0274, 0101.C-0275, 0101.C-0379, 0101.C-0407, 0101.C-0497, 0101.C-0510, 0101.C-0516, 0101.C-0623, 0101.C-0788, 0101.C-0829, 0101.C-0889, 0101.D-0091, 0101.D-0465, 0101.D-0494, 0101.D-0697, 0102.A-0697, 0102.C-0171, 0102.C-0319, 0102.C-0338, 0102.C-0414, 0102.C-0451, 0102.C-0525, 0102.C-0558, 0102.C-0584, 0102.C-0618, 0102.C-0812, 0102.D-0119, 0102.D-0281, 0102.D-0483, 0102.D-0596, 0103.C-0206, 0103.C-0240, 0103.C-0432, 0103.C-0442, 0103.C-0472, 0103.C-0548, 0103.C-0719, 0103.C-0759, 0103.C-0785, 0103.C-0874, 0103.D-0445, 0104.C-0090, 0104.C-0358, 0104.C-0413, 0104.C-0418, 0104.C-0588, 0104.C-0849, 0104.C-0863, 072.A-0244, 072.C-0096, 072.C-0488, 072.C-0513, 072.C-0636, 072.D-0286, 072.D-0419, 072.D-0707, 073.A-0041, 073.C-0733, 073.C-0784, 073.D-0038, 073.D-0136, 073.D-0527, 073.D-0578, 073.D-0590, 074.C-0012, 074.C-0037, 074.C-0061, 074.C-0102, 074.C-0221, 074.C-0364, 074.D-0131, 074.D-0380, 075.C-0087, 075.C-0140, 075.C-0202, 075.C-0234, 075.C-0332, 075.C-0689, 075.C-0710, 075.C-0756, 075.D-0194, 075.D-0600, 075.D-0614, 075.D-0760, 075.D-0800, 076.C-0010, 076.C-0073, 076.C-0155, 076.C-0279, 076.C-0429, 076.C-0878, 076.D-0103, 076.D-0130, 076.D-0158, 076.D-0207, 077.C-0012, 077.C-0080, 077.C-0101, 077.C-0295, 077.C-0364, 077.C-0513, 077.C-0530, 077.D-0085, 077.D-0498, 077.D-0633, 077.D-0720, 078.C-0037, 078.C-0044, 078.C-0133, 078.C-0209, 078.C-0233, 078.C-0403, 078.C-0510, 078.C-0751, 078.C-0833, 078.D-0067, 078.D-0071, 078.D-0245, 078.D-0299, 078.D-0492, 079.C-0046, 079.C-0127, 079.C-0170, 079.C-0329, 079.C-0463, 079.C-0657, 079.C-0681, 079.C-0828, 079.C-0898, 079.C-0927, 079.D-0009, 079.D-0075, 079.D-0118, 079.D-0160, 079.D-0462, 079.D-0466, 080.C-0032, 080.C-0071, 080.C-0581, 080.C-0664, 080.C-0712, 080.D-0047, 080.D-0086, 080.D-0151, 080.D-0318, 080.D-0347, 080.D-0408, 081.C-0034, 081.C-0119, 081.C-0148, 081.C-0211, 081.C-0388, 081.C-0774, 081.C-0779, 081.C-0802, 081.C-0842, 081.D-0008, 081.D-0065, 081.D-0066, 081.D-0109, 081.D-0531, 081.D-0610, 081.D-0870, 082.B-0610, 082.C-0040, 082.C-0212, 082.C-0308, 082.C-0312, 082.C-0315, 082.C-0333, 082.C-0357, 082.C-0390, 082.C-0412, 082.C-0427, 082.C-0608, 082.C-0718, 082.D-0499, 082.D-0833, 083.C-0186, 083.C-0413, 083.C-0627, 083.C-0794, 083.C-1001, 083.D-0040, 083.D-0549, 083.D-0668, 083.D-1000, 084.C-0185, 084.C-0228, 084.C-0229, 084.C-1024, 084.C-1039, 084.D-0338, 084.D-0591, 085.C-0019, 085.C-0063, 085.C-0318, 085.C-0393, 085.C-0614, 085.D-0296, 085.D-0395, 086.C-0145, 086.C-0230, 086.C-0284, 086.C-0448, 086.D-0078, 086.D-0240, 086.D-0657, 087.C-0012, 087.C-0368, 087.C-0412, 087.C-0497, 087.C-0649, 087.C-0831, 087.C-0990, 087.D-0511, 087.D-0771, 087.D-0800, 088.C-0011, 088.C-0323, 088.C-0353, 088.C-0513, 088.C-0662, 088.D-0066, 089.C-0006, 089.C-0050, 089.C-0151, 089.C-0415, 089.C-0497, 089.C-0732, 089.C-0796, 089.D-0138, 089.D-0302, 089.D-0383, 090.C-0131, 090.C-0395, 090.C-0421, 090.C-0540, 090.C-0849, 090.D-0256, 091.C-0034, 091.C-0184, 091.C-0271, 091.C-0438, 091.C-0456, 091.C-0471, 091.C-0844, 091.C-0853, 091.C-0866, 091.C-0936, 091.D-0469, 091.D-0759, 091.D-0836, 092.C-0282, 092.C-0427, 092.C-0454, 092.C-0579, 092.C-0715, 092.C-0721, 092.C-0832, 092.D-0206, 092.D-0261, 092.D-0363, 093.C-0062, 093.C-0163, 093.C-0184, 093.C-0376, 093.C-0409, 093.C-0417, 093.C-0423, 093.C-0474, 093.C-0540, 093.C-0919, 093.D-0367, 093.D-0833, 094.C-0090, 094.C-0297, 094.C-0322, 094.C-0428, 094.C-0790, 094.C-0797, 094.C-0894, 094.C-0901, 094.C-0946, 094.D-0056, 094.D-0274, 094.D-0596, 094.D-0704, 095.C-0040, 095.C-0105, 095.C-0367, 095.C-0551, 095.C-0718, 095.C-0799, 095.C-0947, 095.D-0026, 095.D-0155, 095.D-0194, 095.D-0269, 095.D-0717, 096.C-0053, 096.C-0082, 096.C-0183, 096.C-0210, 096.C-0331, 096.C-0417, 096.C-0460, 096.C-0499, 096.C-0657, 096.C-0708, 096.C-0762, 096.C-0876, 096.D-0064, 096.D-0072, 096.D-0257, 096.D-0402, 097.C-0021, 097.C-0090, 097.C-0277, 097.C-0390, 097.C-0434, 097.C-0561, 097.C-0571, 097.C-0864, 097.C-0948, 097.C-1025, 097.D-0120, 097.D-0150, 097.D-0156, 097.D-0420, 098.C-0042, 098.C-0269, 098.C-0292, 098.C-0304, 098.C-0366, 098.C-0440, 098.C-0446, 098.C-0518, 098.C-0645, 098.C-0739, 098.C-0820, 098.C-0860, 098.D-0187, 099.C-0081, 099.C-0093, 099.C-0138, 099.C-0205, 099.C-0303, 099.C-0304, 099.C-0334, 099.C-0374, 099.C-0458, 099.C-0491, 099.C-0599, 099.C-0798, 099.C-0880, 099.C-0898, 099.D-0236, 099.D-0380, 105.2045.001, 105.2045.002, 105.207T.001, 105.208G.001, 105.20AK.002, 105.20AZ.001, 105.20B1.003, 105.20FX.001, 105.20G9.001, 105.20GX.001, 105.20L0.001, 105.20L8.002, 105.20MP.001, 105.20N0.001, 105.20NV.001, 105.20PH.001, 106.20Z1.001, 106.20Z1.002, 106.212H.001, 106.212H.007, 106.212H.009, 106.212H.010, 106.215E.001, 106.215E.002, 106.215E.004, 106.216H.001, 106.21DB.001, 106.21DH.001, 106.21ER.001, 106.21GB.003, 106.21MA.001, 106.21PJ.001, 106.21PJ.002, 106.21R4.001, 106.21TJ.001, 106.21TJ.008, 107.22R1.001, 107.22UN.001, 108.21XB.001, 108.21YY.001, 108.21YY.002, 108.21YY.004, 108.21YY.005, 108.222V.001, 108.2271.001, 108.2271.002, 108.2271.003, 108.229Z.001, 108.229Z.002, 108.22A8.001, 108.22CE.001, 108.22E7.001, 108.22KV.001, 108.22KV.002, 108.22KV.003, 108.22KV.004, 108.22KV.005, 108.22L8.001, 108.22LE.001, 108.22LR.001, 108.23MM.004, 108.23MM.005, 109.230J.001, 109.2317.001, 109.233Q.001, 109.2374.001, 109.2392.001, 109.239V.001, 109.23J8.001, 110.23XW.001, 110.23XW.002, 110.23YQ.001, 110.241K.001, 110.241K.002, 110.242T.001, 110.2434.001, 110.2438.001, 110.2460.001, 110.248C.001, 110.24BB.001, 110.24C8.001, 110.24C8.002, 110.24D8.001, 1101.C-0557, 1101.C-0721, 1102.C-0249, 1102.C-0339, 1102.C-0923, 1102.D-0954, 111.24PJ.002, 111.24UR.001, 111.24ZQ.001, 111.24ZW.001, 111.250B.001, 111.254A.001, 111.254E.001, 111.254R.002, 111.255C.001, 111.255C.003, 111.255C.004, 111.263V.001, 111.264X.001, 180.C-0886, 182.D-0356, 183.C-0437, 183.C-0972, 183.D-0729, 184.C-0639, 184.C-0815, 185.D-0056, 187.D-0917, 188.C-0265, 188.C-0779, 190.C-0027, 190.D-0237, 191.C-0505, 191.C-0873, 191.D-0255, 192.C-0224, 192.C-0852, 196.C-0042, 196.C-1006, 198.C-0169, 198.C-0836, 198.C-0838, 2101.C-5015, 276.C-5009, 281.D-5052, 281.D-5053, 281.D-5054, 282.C-5034, 282.C-5036, 282.D-5006, 283.C-5017, 283.C-5022, 288.C-5010, 289.C-5053, 289.D-5015, 292.C-5004, 295.C-5031, 295.C-5035, 297.C-5051, 495.L-0963, 60.A-9036, 60.A-9109, 60.A-9501, 60.A-9700, 60.A-9709.

This work has made use of data from the European Space Agency (ESA) mission *Gaia* (https://www.cosmos.esa.int/gaia), processed by the *Gaia* Data Processing and Analysis Consortium (DPAC, https://www.cosmos.esa.int/web/gaia/dpac/consortium). Funding for the DPAC has been provided by national institutions, in particular the institutions participating in the *Gaia* Multilateral Agreement.

Table 4: Updated HARPS-RVBank. The dots represent the rest of the columns from the previous version (Trifonov et al. 2020). The full table is available on the CDS. The mflag column denotes stars for which metallicity could not be determined.

Name	RA [°]	Dec [°]	BJD [d]	...	R'_{HK}	$\Delta R'_{HK}$	$vflag$	$mflag$
BD+012494	163.0321195	0.49329	2458249.6510659	...	1.60E-5	1.15E-6	0	0
BD+012494	163.0321195	0.49329	2458251.5921099	...	1.43E-5	9.92E-7	0	0
BD+012494	163.0321195	0.49329	2458262.4807279	...	1.70E-5	1.04E-6	0	0
BD+012494	163.0321195	0.49329	2458263.543513	...	6.60E-6	1.11E-6	0	0

References

Amado, P. J., Bauer, F. F., Rodríguez López, C., et al. 2021, A&A, 650, A188
Bashi, D., Zucker, S., Adibekyan, V., et al. 2020, A&A, 643, A106
Binnenfeld, A., Shahaf, S., Anderson, R. I., & Zucker, S. 2021, arXiv e-prints, arXiv:2111.02383
Brems, S. S., Kürster, M., Trifonov, T., Reffert, S., & Quirrenbach, A. 2019, A&A, 632, A37
Collier Cameron, A., Ford, E. B., Shahaf, S., et al. 2021, MNRAS, 505, 1699
Collier Cameron, A., Mortier, A., Phillips, D., et al. 2019, MNRAS, 487, 1082
Courcol, B., Bouchy, F., Pepe, F., et al. 2015, A&A, 581, A38
Dumusque, X., Udry, S., Lovis, C., Santos, N. C., & Monteiro, M. J. P. F. G. 2011, A&A, 525, A140
Feng, F., Shectman, S. A., Clement, M. S., et al. 2020, ApJS, 250, 29
Fuhrmeister, B., Czesla, S., Perdelwitz, V., et al. 2022, arXiv e-prints, arXiv:2212.03514
Gaia Collaboration, Brown, A. G. A., Vallenari, A., et al. 2021a, A&A, 649, A1
Gaia Collaboration, Luri, X., Chemin, L., et al. 2021b, A&A, 649, A7
Gomes da Silva, J., Santos, N. C., Adibekyan, V., et al. 2021, A&A, 646, A77
Haywood, R. D., Collier Cameron, A., Unruh, Y. C., et al. 2016, MNRAS, 457, 3637
Husser, T. O., Wende-von Berg, S., Dreizler, S., et al. 2013, A&A, 553, A6
Kossakowski, D., Kürster, M., Henning, T., et al. 2022, A&A, 666, A143
Marchwinski, R. C., Mahadevan, S., Robertson, P., Ramsey, L., & Harder, J. 2015, ApJ, 798, 63
Mayor, M., Pepe, F., Queloz, D., et al. 2003, The Messenger, 114, 20
McQuillan, A., Mazeh, T., & Aigrain, S. 2014, ApJS, 211, 24
Palatnick, S., Kipping, D., & Yahalomi, D. 2021, ApJ, 909, L6
Pepe, F., Molaro, P., Cristiani, S., et al. 2014, Astronomische Nachrichten, 335, 8
Perdelwitz, V., Mittag, M., Tal-Or, L., et al. 2021, A&A, 652, A116
Queloz, D., Henry, G. W., Sivan, J. P., et al. 2001, A&A, 379, 279
Reiners, A., Shulyak, D., Anglada-Escudé, G., et al. 2013, A&A, 552, A103
Saar, S. H., Butler, R. P., & Marcy, G. W. 1998, ApJ, 498, L153
Saar, S. H. & Testa, P. 2012, in Comparative Magnetic Minima: Characterizing Quiet Times in the Sun and Stars, ed. C. H. Mandrini & D. F. Webb, Vol. 286, 335–345
Schröder, C., Reiners, A., & Schmitt, J. H. M. M. 2009, A&A, 493, 1099
Soto, M. G. & Jenkins, J. S. 2018, A&A, 615, A76
Soto, M. G., Jones, M. I., & Jenkins, J. S. 2021, A&A, 647, A157
Sreenivas, K. R., Perdelwitz, V., Tal-Or, L., et al. 2021, arXiv e-prints, arXiv:2112.09029
Stassun, K. G., Oelkers, R. J., Paegert, M., et al. 2019, AJ, 158, 138
Tal-Or, L., Trifonov, T., Zucker, S., Mazeh, T., & Zechmeister, M. 2019, MNRAS, 484, L8
Tal-Or, L., Zechmeister, M., Reiners, A., et al. 2018, A&A, 614, A122
Torres, G., Fischer, D. A., Sozzetti, A., et al. 2012, ApJ, 757, 161
Trifonov, T. 2019, The Exo-Striker: Transit and radial velocity interactive fitting tool for orbital analysis and N-body simulations
Trifonov, T., Tal-Or, L., Zechmeister, M., et al. 2020, A&A, 636, A74
Trifonov, T., Wollbold, A., Kürster, M., et al. 2022, AJ, 164, 156
Zechmeister, M., Reiners, A., Amado, P. J., et al. 2018, A&A, 609, A12
Zechmeister, M., Reiners, A., Amado, P. J., et al. 2020, SERVAL: SpEctrum Radial Velocity AnaLyser, Astrophysics Source Code Library, record ascl:2006.011